ChemPubSoc Europe

DOI: 10.1002/ejic.201801173

EurJIC European Journal of Inorganic Chemistry

Full Paper

Fluorescence Bioimaging

Pyrophosphate Prompted Aggregation-Induced Emission: Chemosensor Studies, Cell Imaging, Cytotoxicity, and Hydrolysis of the Phosphoester Bond with Alkaline Phosphatase

Pushap Raj,[a] Amanpreet Singh,[a] Ajnesh Singh,[b] Ashutosh Singh,[d] Neha Garg,[d] Navneet Kaur,*[c] and Narinder Singh*[a]

Abstract: Two benzimidazole-based zinc complexes $[(Zn)_2(L2)_2Cl_2(DMSO)_2]$ (**R1**) and $[Zn(L2)_2(NO_3)_2(H_2O)_2]$ (**R2**) were synthesized and characterized with various spectroscopic data. The single X-ray structure determination reveals that complex **R1** is dinuclear and tetrahedral in geometry, while complex **R2** is mononuclear and octahedral in geometry. Further, both zinc complexes were investigated for pyrophosphate sensing in an aqueous medium. Complex **R1** is found to be selective towards pyrophosphate; it leads to 5.5-fold enhancement in the emission intensity due to aggregation-induced emission. However, complex **R2** has shown binding with all, ATP, AMP, ADP, and pyrophosphate, which is attributed to the chelate effect. Consequently, complex **R1** was utilized for the intracellular detection of pyrophosphate in HeLa cells. Furthermore, the PPi based zinc complex **R1** is also used as a bio-analytical tool to construct a real-time fluorescence assay for the enzymatic activity of alkaline phosphatases (ALP).

Introduction

The detection and quantification of inorganic phosphates are crucial because of their role in many environmental and biological processes.[1–4] Pyrophosphate is a dimeric form of inorganic phosphate which has a decisive role in the cellular metabolic process, real-time DNA sequencing, energy storage, signal transduction, ATP hydrolysis, and calcium pyrophosphate deposition etc.[4–8] Moreover, pyrophosphate has become an indispensable biomarker for diagnosis of numerous diseases like chondrocalcinosis, arthritis, and cancer.[9–12] Therefore, the detection of PPi is an important criterion to establish the disease state under physiological conditions.

The most predominant strategies reported for the detection of pyrophosphate are based on hydrogen bonding interaction, charged transfer, pyrophosphate metal complex formation and metal displacement assay.[13–17] The binding sites available in these approaches are directly or indirectly linked to fluorophore unit through covalent bonding and afford a direct signal response on interaction with PPi.[18–20] The available organic receptors make use of binding sites such as urea/thiourea, amide, pyrazole and imidazolium derivative; and hence only operative in a purely organic or semi-organic solvent.[5,21,22] Pyrophosphate recognition in physiological condition is still a challenging task due to competition for the binding site between solvent and the target analyte.[23,24] Moreover, to explore the application of sensor for bio-analytical measurements; the sensor system should be operative in an aqueous medium. Consequently, most of the sensors which are fabricated with organic moieties exhibit a restricted solubility in aqueous medium and impede the application of sensor in bio-analytical techniques.[25,26]

To overcome these constraints, aggregation-induced emission (AIE) is an important phenomenon for sensing of pyrophosphate in an aqueous medium, even using the organic moieties for sensors.[27] The AIE phenomenon was first invented with the pioneering work of Tang et al. in 2001, for 1,1-dimethyl-2,3,4,5-tetraphenylsilole and tetraphenylethene (TPE) molecules.[28] The tetraphenylsilole molecules are non-emissive or weakly fluorescent in molecular state. However, in the aggregate state, these compounds offer strong emission; most probably through the restriction of non-radiative decay from the excited state.[29] The success of AIE encouraged the researchers to synthesized various probe based on AIE phenomenon and used for the application like organic light-emitting diodes, chemo/bio-sensors and biological cell imaging.[30–33] Owing to the simplicity and efficiency, AIE becomes one of the promising strategies for sensing of environmentally and biologically important analytes in the aqueous medium.[34] To the best of our understanding, there are only a few reports available for sensing of pyrophosphate based on AIE approach. Rissanen et al. have employed the self-assembled terpyridine-Zn^{2+}complex

[a] *Department of Chemistry, Indian Institute Technology Ropar, Punjab, 140001, India*
E-mail: nsingh@iitrpr.ac.in
[b] *Department of Applied Sciences and Humanities, Jawaharlal Nehru Govt. Engineering College, Sundernagar, Mandi, Himachal Pradesh 175018, India*
[c] *Department of Chemistry, Panjab University Chandigarh, Chandigarh, 160014, India*
E-mail: navneetkaur@pu.ac.in
[d] *School of Basic Sciences, Indian Institute of Technology Mandi, Kamand, Mandi, Himachal Pradesh 175005, India*
Supporting information and ORCID(s) from the author(s) for this article are available on the WWW under https://doi.org/10.1002/ejic.201801173.

for nanomolar detection of pyrophosphate in water.[35] Ni et al. have also used the terpyridine-Zn^{2+} complex for selective and sensitive detection of pyrophosphate under a physiological condition which is also based on AIE phenomenon.[36]

In the present manuscript, we have explored AIE approach for pyrophosphate sensing under physiological condition using benzimidazole-based zinc complexes **R1** and **R2,** respectively. Both the zinc complexes were prepared by reaction of zinc chloride and zinc nitrate to the respective ligand **L1** and **L2,** which yielded dinuclear (**R1**) and mononuclear zinc complex (**R2**). The prepared dinuclear and mononuclear benzimidazole-based zinc complexes are utilized for selective sensing of pyrophosphate in an aqueous medium. The pyrophosphate has strong tendency to coordinate with zinc metal ions by replacing labile anions/solvent and shown modulation in the emission spectrum of zinc complexes (**R1-2**).[37–39] The zinc complex **R1** was further utilized for pyrophosphate sensing in the HeLa cells imaging and also evaluated for their cytotoxic activity. Moreover, we have developed pyrophosphate based zinc complex for bio-analytical tool to extend the real-time activities for alkaline phosphatase enzyme.[40,41]

Alkaline phosphatase is a homodimeric metalloenzyme containing two zinc atom in its structural unit, which are decisive for its catalytical role.[42] The enzyme is active in the basic environment and regulates the hydrolysis of monophosphate ester into inorganic phosphate and alcohol.[43–45]It is accounted that the deprotonated hydroxyl group of serine moiety of ALP enzyme undergo nucleophilic attack to a phosphate group and hydrolyze the phosphate ester bond.[46] The ALP enzyme hydrolytically promotes the breakdown of phosphate ester bond of various molecules like alkaloids, nucleotides, and protein through the nucleophilic attack.[47] Some of the recent reports have suggested that the interaction between $Zn^{2+}$and non-bridging phosphorus-oxygen group lead to enhancement of ALP catalyzed phosphate ester bond cleavage. Although, the role of zinc ion for the binding of phosphorus-oxygen bond and cleavage of phosphate ester bond through ALP was not well recognized.[42]However, there are few reports available in the literature; which explored the enzymatic role of ALP for hydrolyzing the phosphate ester bond by monitoring the modulation in the emission intensity of the molecular sensor.[48] Therefore, the present sensor is used for monitoring of ALP activities through modulation in the fluorescence intensity.

Result and Discussion

Synthesis and Characterization of Ligands and Metal Complexes

Ligands **L1-2** were synthesized through the condensation reaction between *o*-phenylenediamine and 4-pyridinecarboxaldehyde as shown in Scheme 1. It is important to mention here that the reactants under dilute conditions afford the formation of **L1**. The structural formulae of both the ligands **L1-2** were elucidated with spectroscopic data such as ^{1}H NMR, ^{13}C NMR, FTIR and mass spectrometry (Figure S1–S8**)**. The ^{1}H NMR spectrum of **L1** has shown the formation of imine linkage; while the ^{1}H NMR spectrum of **L2** indicates the formation of benzimidazole moiety. Further, the mass spectra of ligands **L1** and **L2** have exhibited *m/z* peak at 198.04 and 196.02 respectively, which confirmed the molecular ion peak [M + H] of the structures of **L1-2**.

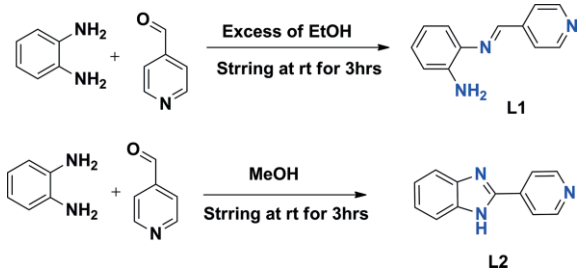

Scheme 1. Synthesis of ligands **L1-2**.

Finally, our attempts remained successful to grow the crystals of ligand **L1** (in ethanol); which confirmed the structure of **L1** through single X-ray crystallography (Figure 1A**)**. The complex **R1** was synthesized from **L1** in methanol/DMSO solvent system, while complex **R2** was synthesized from **L2** in MeOH: THF solvent system as shown in Scheme 2. Both the complexes were characterized with spectroscopic method of analysis (Figure S9–S12) and the structures were authenticated with single X-ray crystallography. The comparison of ^{1}H NMR spectra of **L1** and **R1** (both recorded in [D_6]DMSO) revealed that the imine-linked structure of **L1** has been converted into the benzimidazole moiety. We have already reported the mechanism for the formation of benzimidazole moiety from similar type of substrates. Further, the sp^2 nitrogen of benzimidazole moiety seems to coordinate with Zn(II) leading to locking of benzimidazole tautomerism. Consequently, this directed the splitting in aromatic signals of benzimidazole as evident from ^{1}H NMR spectrum of **R1** (Figure S9).[49,50] Similarly, the ^{1}H NMR spectrum of complex **R2** in [D_6]DMSO displayed the shift in aromatic signals of pyridine moiety by $\Delta\delta$ = 0.04-0.06 ppm and also confirmed the formation of zinc complex (Figure S10). The crystallinity of the bulk samples of **R1-2** was established from the comparison of powder XRD pattern and the simulated data obtained from mercury software as shown in Figure S16–S17. The result of powder XRD pattern was similar to the simulated data, which confirm the phase purity of complexes in the solid state. The photophysical properties of **R1-2** complexes were recorded through UV/Visible absorption and emission spectroscopy in the aqueous solvent system. The 10 μM solution of **R1** shows absorption maxima at 310 nm with molar absorption value of $\varepsilon_0 = 2.8 \times 10^4$ L·mol^{-1} cm^{-1}and assigned to π–π* transition of ligand **L1**. Similarly, the complex **R2** demonstrates absorption maxima at 315 nm ($\varepsilon_0 = 1.2 \times 10^4$ L·mol^{-1} cm^{-1}) and again due to π–π* transition of the ligand as shown in Figure S18A–B.[51] Both the complexes **R1** and **R2** were excited at 310 and 315 nm respectively and exhibit emission at 487 and 485 nm with low quantum yield (Φ = 0.10 and 0.08) respectively.[51] The weak fluorescence emission of complex **R2** is due to free rotation across single bond connecting the pyridyl and benzimidazole segments of the molecules and thus, leads to nonradiative decay.

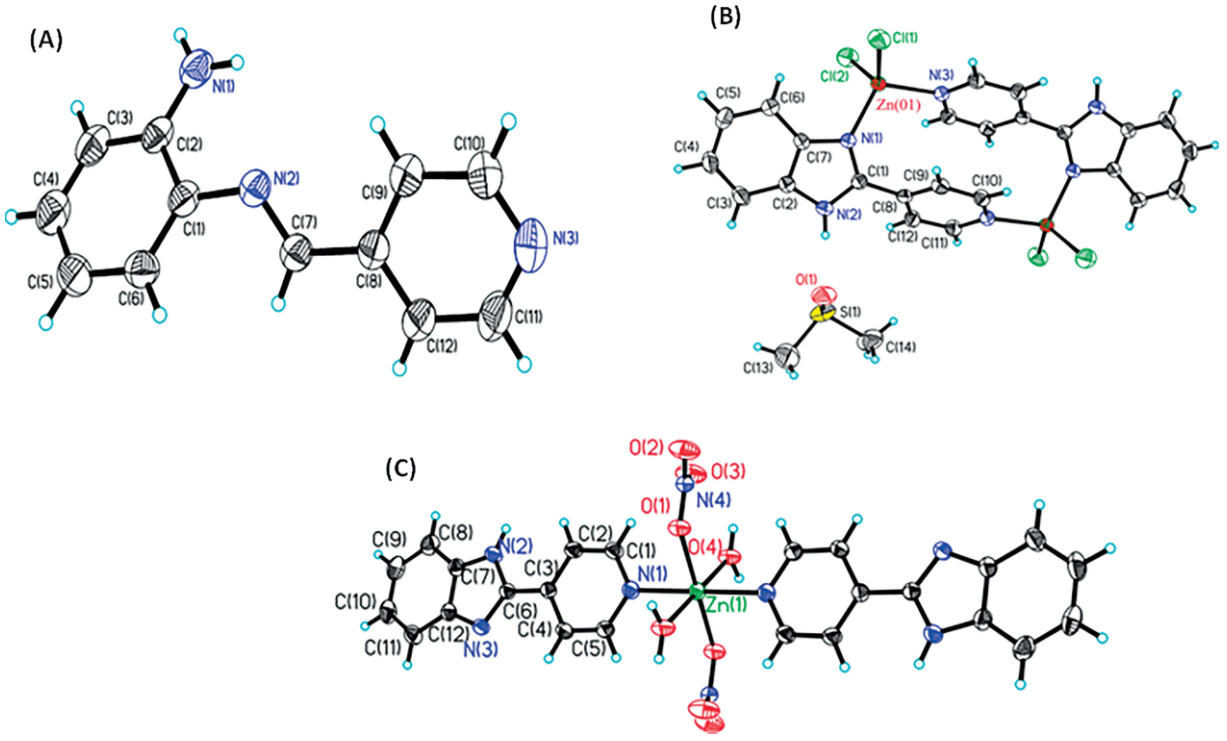

Figure 1. ORTEP diagram along with atom numbering scheme with 40 % probability thermal ellipsoids: (A) **L1**, (B) **R1,** (C) **R2**.

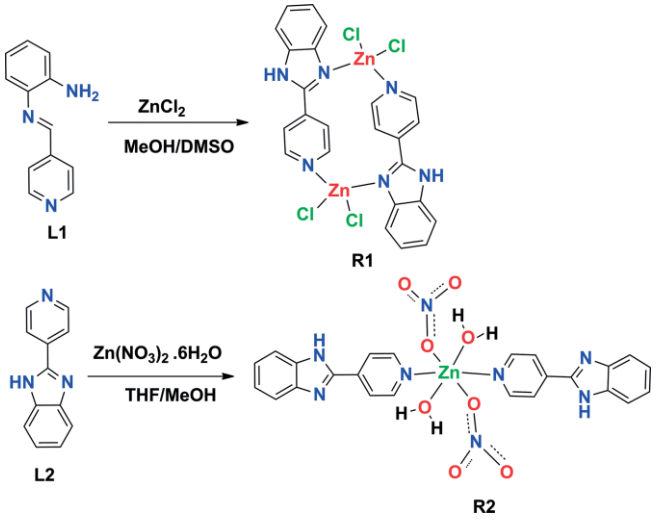

Scheme 2. Synthesis of zinc complexes **R1-2**.

Structure Description

Ligand **L1** crystallizes in orthorhombic crystal system with *Fdd*2 space group, and the asymmetric unit contains one moiety of Ligand **L1**. Figure 1 (A) shows the ORTEP diagram along with atom numbering scheme of the ligand **L1**. The 2-aminobenzene and pyridyl moieties are not coplanar; both planes have a dihedral angle of 46.63°. The selected bond lengths and bond angles are given in Table S2. The moieties of ligand **L1** arranged in the form of one-dimensional chain running along c-axis. Different moieties in these chains are joined together by N-H•N hydrogen bonds. Two such chains are packed in double helical type as shown in Figure S13.

The complex **R1** crystallizes in monoclinic crystal system with $P2_1/c$ space group. The asymmetric unit consists of one moiety of complex $[(C_{14}H_{15}N_3)_2Cl_2Zn_2]$ and two molecules of dimethylsulfoxide (DMSO) as a solvent of crystallization. The Zn(II) has tetrahedral coordination which is satisfied by two chloride ions and two nitrogen atoms originating from benzimidazole and pyridyl moieties. The ORTEP diagram along with atom numbering scheme is shown in Figure 1(B). The selected bond lengths and bond angles are given in Table 1. In the crystal lattice, the molecules are interacting with each other by different type of hydrogen bonding interactions (N-H···O, C-H···O, and C-H···Cl). The solvent molecules are acting as linkers between different moieties of complex **R1.** This arrangement of molecules in the crystal lattice along c-axis is given in Figure S14.

Single crystal X-ray structure determination of complex **R2** was undertaken to establish the structure unambiguously. X-ray structure determination revealed that complex **R2** crystallizes in triclinic crystal system with space group $P\bar{1}$ and consists of one molecule of complex **R2**.

The central Zn(II) metal ion is attained slightly distorted octahedral geometry. Octahedral coordination around central metal ion completed by two nitrogen atoms originating from ligand **L2** and four oxygen atoms, two each originating from nitrate ions and water molecules. The ORTEP diagram along with atom numbering scheme of the complex is shown in Figure 1C. The selected bond lengths and bond angles are given in Table 2. In the crystal lattice, different moieties are interacting with each other through O/N-H···O, H/O-H···N and C-H···O hydrogen

Table 1. Selected bond lengths and angles (Å (°)) for complex **R1**.

Bond lengths (Å)					
Zn(1)–N(1)	2.037(2)	Zn(1)–Cl(1)	2.2237(9)	N(2)–C(1)	1.340(4)
Zn(1)–N(3)	2.061(2)	N(1)–C(1)	1.326(3)	N(2)–C(2)	1.376(4)
Zn(1)–Cl(2)	2.2233(9)	N(1)–C(7)	1.399(4)	N(3)–C(11)	1.331(4)
Bond angles (°)					
N(1)–Zn(1)–N(3)	111.08(9)	N(3)–Zn(1)–Cl(1)	107.66(7)	C(7)–N(1)–Zn(1)	119.67(18)
N(1)–Zn(1)–Cl(2)	108.80(7)	Cl(2)–Zn(1)–Cl(1)	116.50(4)	C(1)–N(2)–C(2)	107.5(2)
N(3)–Zn(1)–Cl(2)	103.93(7)	C(1)–N(1)–C(7)	104.8(2)	C(1)–N(2)–H(2A)	126.2
N(1)–Zn(1)–Cl(1)	108.78(7)	C(1)–N(1)–Zn(1)	133.96(19)	C(2)–N(2)–H(2A)	126.2

Table 2. Selected bond lengths and angles (Å (°)) for complex **R2**.

Bond lengths (Å)					
Zn(1)–N(1)	2.0991(12)	O(1)–N(4)	1.2473(15)	N(1)–C(5)	1.3428(19)
Zn(1)–O(4)	2.1217(10)	O(2)–N(4)	1.2312(17)	N(2)–C(6)	1.3576(18)
Zn(1)–O(1)	2.2025(11)	O(3)–N(4)	1.2387(17)	N(2)–C(7)	1.3708(19)
		N(1)–C(1)	1.3389(19)	N(3)–C(6)	1.3207(18)
Bond angles (°)					
N(1)#1-Zn(1)–N(1)	180.0	O(4)–Zn(1)–O(4)#1	180.0	O(4)#1-Zn(1)–O(1)	78.93(4)
N(1)#1-Zn(1)–O(4)	88.63(5)	N(1)#1-Zn(1)–O(1)	86.79(4)		
N(1)–Zn(1)–O(4)	91.37(4)	N(1)–Zn(1)–O(1)	93.21(4)		
N(1)–Zn(1)–O(4)#1	88.63(5)	O(4)–Zn(1)–O(1)	101.07(4)		

bonding which results in the formation of chains. These chains are held together in crystal lattice through some C-H···O hydrogen bonds. The coordinated nitrate ions and water are acting as linkers between different moieties and resulting in a robust 3-D crystal structure. The packing diagram of compound **R2** is shown in Figure S15. The hydrogen bonding parameters are given in Table S5.

Aqueous and Thermal Stability of the Complexes

^{1}H NMR spectroscopy and XRD analysis were employed to evaluate the aqueous stability of the zinc complexes **R1**-**2**. The ^{1}H NMR spectrum of **R1** recorded in D_2O show signals at δ = 8.63, 7.96, 7.56 (split), 7.28 ppm corresponding to aromatic protons of **R1** (Figure S19). It has been envisaged that the coordination of Zn(II) with benzimidazole nitrogen restrict the rapid tautomerism of hydrogen atom across N-1 and N-3. The locking of tautomer in particular state split the aromatic signals of benzimidazole moiety. The complex **R2** shows proton signals at δ = 8.51, 7.80, 7.49 and 7.20 ppm corresponding to aromatic protons of the **R2** as shown in Figure S20. Further, the ^{1}H NMR of both the complexes was recorded on alternative days till ten days and no significant changes were observed. Hence, it is evident from^{1}H NMR spectrum that both the complexes are stable in an aqueous medium. Moreover, both zinc complexes were suspended in water for ten days and after that the powder XRD pattern was recorded (Figure S16–S17) which shows that the complexes remain stable after suspending them in aqueous medium for long duration. The thermal studies of **R1**-**2** were analyzed through TGA in the temperature range of 25 to 700 °C at a heating rate of 10 °C per minute under nitrogen environment**.** The complex **R1** is stable up to ca 220 °C, after this temperature the progressive decomposition of the complex occurred. The organic ligand completely decomposes at 450 °C with the loss of 60 % weight of the complex. The 40 % black color residue remains at the end of the heating process which contains ZnO and carbonaceous matter. Similarly, the **R2** complex start decomposing from 200 °C and complete decomposition of ligand take place at 360 °C with the loss of 55 % of the mass of the complex. The remained black residue contains ZnO and carbonaceous materials. Thus, TGA studies confirm that both zinc complexes are crystalline and display thermal stability at the room temperature (Figure S21**)**.

Chemosensor Activity of Zinc Complexes R1 and R2

The emission spectroscopy was employed to study the chemosensor activity of both zinc complexes with the library of anions. The fixed concentration of zinc complexes (10 μM) was prepared in an aqueous medium (HEPES buffer at pH = 7.4) and used for recognition studies. The 10 μM solution of **R1** was excited at 310 nm, and emission was obtained at 487 nm with low quantum yield (Φ = 0.10). To investigate the anion binding behavior of complex the emission spectra of **R1** was recorded on the addition of various anions (30 μM) namely as ATP, ADP, AMP, NADP, NAD, Phosphate, fluoride, carbonate, sulfate, nitrate, hydrogen phosphate, pyrophosphate, bromide, iodide, cyanide, hydroxide, chlorate and sulfide ions. The significant change in

the emission intensity of **R1** was occurred in the presence of pyrophosphate. However, the other anions used did not showed any significant shift in the emission spectrum of **R1**. Upon addition of 30 μM of pyrophosphate, the emission intensity of **R1** was enhanced 5.5-fold at 487 nm with high quantum yield (Φ = 0.29) as shown in Figure 2A. The enhancement in emission intensity confirms the selective binding of pyrophosphate with the coordination sphere of zinc complex. The modulation in emission intensity was due to "aggregation-induced emission", which provides structural rigidity in the complex.[52,53] Furthermore, the titration experiment was performed to confirm the reproducibility of the experiment. In titration experiment; the successive addition of PPi (0-30 μM) to the **R1** solution was carried out, and emission intensity was recorded. The fluorescence titration experiment shows the linear enhancement in fluorescence intensity with increase in the concentration of the pyrophosphate (Figure 2B). Further, to find out the practical utility of the sensor system, the interference experiment was conducted (Figure 2D). In this typical study, the library of anion solutions were added to **R1** along with the pyrophosphate solution and emission was noted. The competitive binding assay demonstrates that no interference was observed for detection of pyrophosphate. HyperSpec Software was used to determine the stability constant between **R1** and PPi. The fluorescence titration data was fitted into HyperSpec software, multiple binding models was applied and a good fit of data was obtained in Figure 2C. In the species distribution curve, the 1:2 species was dominant in a solution state. The fitting data provided log *K* values of 3.21 ± 0.02, 8.74 ± 0.04 and 11.21 ± 0.05 for 1:1, 1:2 and 2:1 complex, respectively.[54,55] The detection limit of PPi sensing was calculated through IUPAC reported 3σ method, and it came out to be 25 nM.[54]

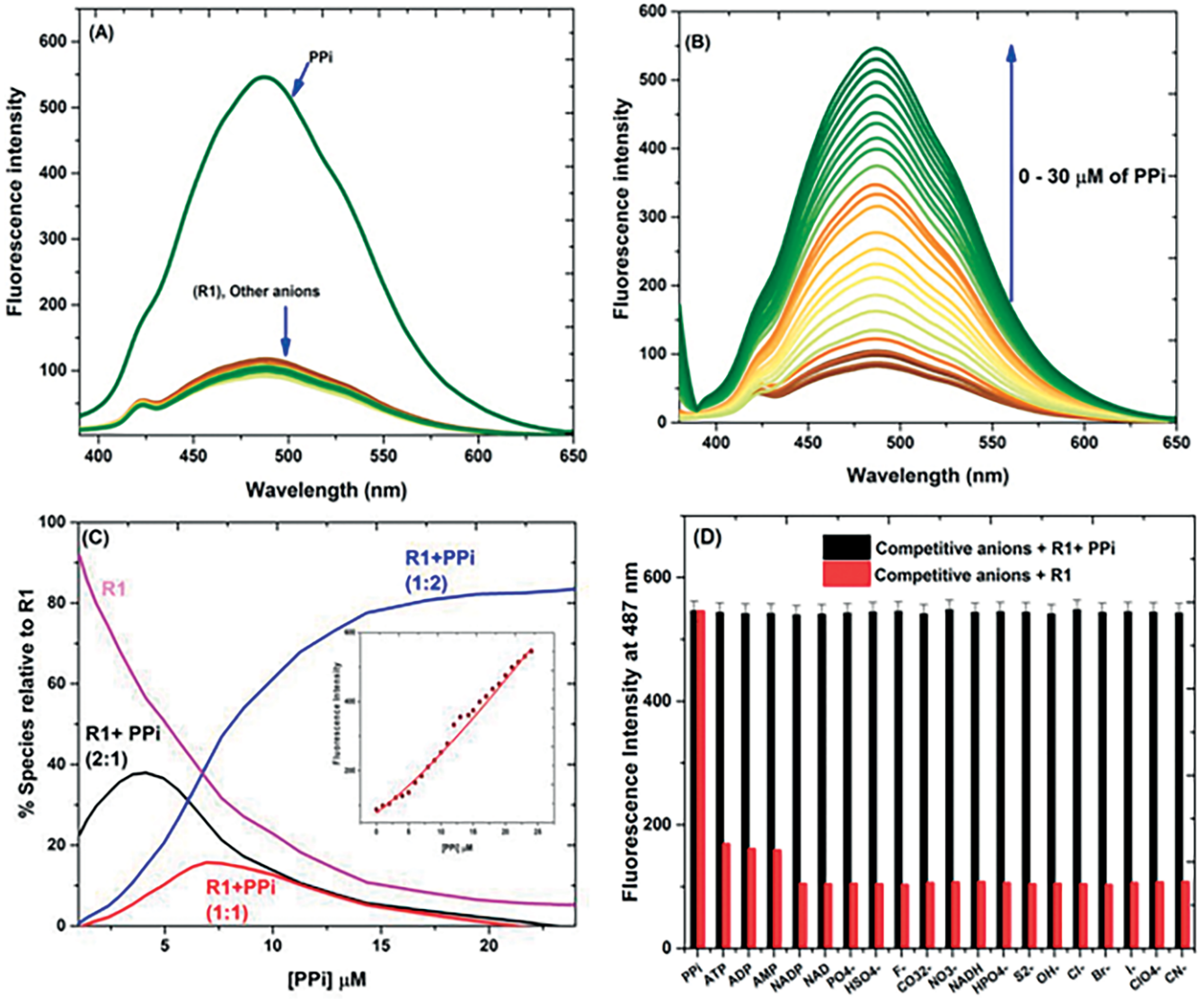

Figure 2. (A) The emission spectra of **R1**(10 μM, λ_{ex} = 310 nm, HEPES buffer, pH = 7.4 at room temperature) at λ_{em} = 487 nm on treatment with various anions (30 μM) in aqueous solution. (B) Fluorescence titration of **R1**(10 μM, HEPES buffer, pH = 7.4) in the presence of PPi (0 -30 μM) at room temperature. (C) Fitting of fluorescence titration data to determine the stability constant between **R1** and PPi with HyperSpec software. (D) The interference studies of complex **R1** for selective detection of PPi in the presence of various anions.

Similarly, the complex **R2** was excited at 315 nm and exhibit emission intensity at 485 nm with low quantum yield (Φ = 0.08). The chemosensor study of **R2** complex was tested with a similar type of analyte as utilized for the complex **R1**. The result of emission experiment shows that **R2** binds with ATP, ADP, AMP,and pyrophosphate. However, the binding pattern toward PPi was more significant than the other nucleotides (Figure S22A**)**. The fluorescence binding mechanism seems to be governed by the chelate effect; as all nucleotide and PPi form chelation with complex **R2.** Upon addition of 0-30 μM of PPi to complex, the emission intensity was enhanced with an increase in the concentration of the analyte (Figure S22B**)**. The interference experiment was performed, and the result showed that the nucleotides interfere with the recognition of PPi (Figure S22D**)**. The stability constant between **R2** and PPi was determined by the similar method as used in complex **R1**. The fitting data showed that 1:2 species was dominant in the complex equilibria having log *K* value of 6.34 ± 0.05 (Figure S22C**)**. The different binding behavior of these two complexes towards PPi may entirely depend upon their distinct geometry, i.e., tetrahedral and octahedral. The **R1** complex possesses tetrahedral geometry (stearic hindered) and coordination sphere can easily accommodate the pyrophosphate anion over the ATP, ADP and AMP. Hence, such binding pattern of **R1** with PPi may lead to aggregate formation as shown in Figure S30. However, the **R2** complex is octahedral in geometry and Zn(II) is easily approachable from PPi as well as other phophorylated biomolecules through solvent or anion exchange leading to non-selective binding pattern.

The time-resolved photoluminescence **(**TRPL) measurements were carried out to realize the mechanism of fluorescence enhancement of **R1** in the presence of PPi (Figure S23A). The excited state decay of both zinc complexes and their pyrophosphate complexes were best tail fitted with bi-exponential function. Lifetimes of the individual components, average lifetime and radiative (k_r) and nonradiative (k_{nr}) rate constant of both zinc complexes and the pyrophosphate sensing are summarized in Table S6. The average excited lifetime (τ) of **R1** in the aqueous medium is 3.49 ns; however, on the addition of 30 μM PPi the average excited lifetime of (τ) was detected at 4.53 ns. This large increase in the value of τ was due to aggregation in the complex and lifetime of **R1**+ PPi species become longer.[56] Analogously, the TRPL spectra of 10 μM **R2**complex exhibit average excited lifetime at 3.05 ns, whereas on the addition of 30 μM PPi the fluorescence lifetime has shifted to 3.34 ns. This small change in the lifetime of **R2**+ PPi species confirms the chelation of PPi to **R2** complex (Figure S23B**)**.[57] Further, the radiative and nonradiative rate constant of both zinc complexes and their pyrophosphate complexes were calculated by using Equation (1).

$$\phi = \frac{kr}{kr + knr} and\ \tau = \frac{1}{kr + knr} \qquad (1)$$

Whereas ϕ is the quantum yield, kr and knr are the radiative and non-radiative rate constant, and τ is the lifetime of the complex. The value of the radiative rate constant (kr) for pyrophosphate zinc complexes was more than of its pure zinc complex, and interestingly these results are well sustained with the static fluorescence intensity of pyrophosphate sensor system. The DLS measurements were also carried out to understand the aggregation of **R1** in the presence of an excess of pyrophosphate. The DLS result revealed that on the addition of 5-30 μM of PPi in 10 μM of **R1;** the size of aggregate increases from 200 nm to 1200 nm (Figure 3A). The detailed investigation of the role of pyrophosphate induced aggregation of the **R1** complex was further employed with TEM analysis. The results of TEM analysis provide evidence for aggregate formation in the **R1** complex as in Figure S24. The TEM analysis predicted that the PPi induced aggregations of **R1** are spherical to oval in shape and possess a size of 1.2 μm. The AFM investigation was also performed to confirm the aggregations of **R1** by PPi**.** The AFM studies showed that the nano-aggregates are spherical and have a size distribution of 1.0 μm to 1.5 μm as depicted in Figure 3B and Figure S25. All three-techniques used for characterization of aggregates correlate with each other and exhibit evidence for the role of pyrophosphate to induce aggregation of **R1**.

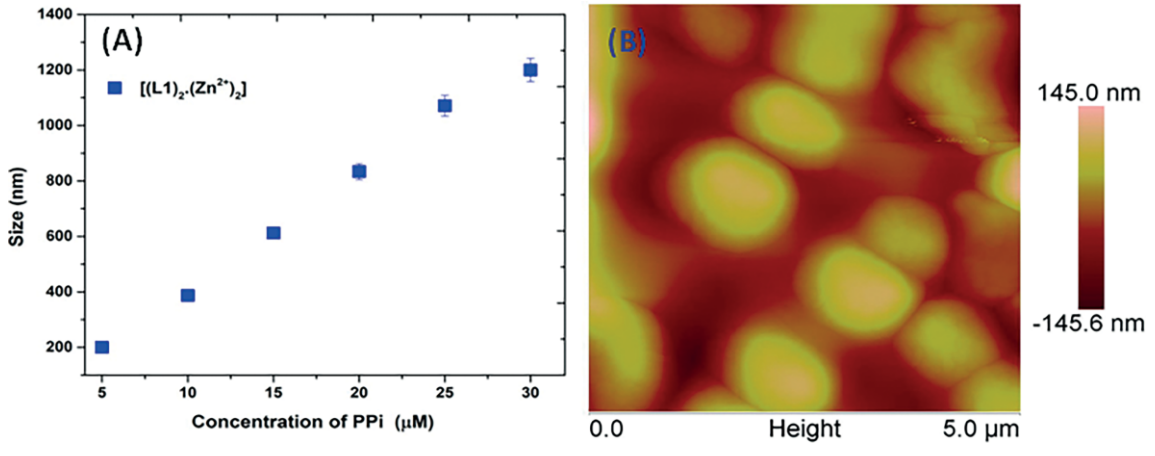

Figure 3. (A) Dynamic light scattering histogram of **R1**+ PPi aggregates showing effect of concentration on the average size of aggregate. (B) AFM measurements of **R1**+ PPi, showing size distribution from 1.0 to 1.5 μm.

The PPi prompted aggregation phenomenon possesses reversibility of **R1**+PPi aggregate, as depicted in Figure S26. The reversibility is the one of the important domains to gratify the demand of a novel chemosensor for reusability of the complex. To scrutinize the reversible binding of **R1** with PPi, the calcium ions have been employed. This is because the Ca(II) has strong affinity to form interaction with pyrophosphate.[58] On addition of 0 - 10 μM of Ca^{2+} to **R1**+ PPi aggregates, the quenching in the fluorescence intensity was observed, this was due to disruption of **R1**+ PPi aggregates and formation of calcium pyrophosphate complex. Thus, it was concluded from the reversibility experiment that the PPi triggered the aggregation-induced emission of **R1** complex and caused enhancement in the emission spectrum. Further turbidimetry method was employed to check whether the aggregates were destroyed or re-dissolved, and the investigation confirmed that the turbid solution of PPi + zinc complex become semi-transparent after addition of 0-10 μM of Ca(II). Further addition of calcium ions did not cause any physical change in the solution. It may be due to the breakdown of PPi+ zinc complex to calcium pyrophosphate and free zinc complex. The DLS studies were further utilized to check the effect of calcium ion on the size of nano-aggregates. The result exhibits that the size of nano-aggregates decreases from 1200 nm to 367 nm (Figure S26B). These studies confirm the reversibility of the sensor system.

Plausible Sensing Mechanism

To study the possible binding mechanism of PPi with **R1** complex, ^{31}P NMR spectroscopy was employed (Figure S27**)**. The ^{31}P NMR spectrum of PPi shows phosphorus signal at -5.83 ppm in D_2O. Upon binding with **R1** complex, the chemical shift value of phosphorus signal got perturbed from -5.83 to -5.34 ppm. This small downfield change in chemical shift value was due to the binding of PPi with the zinc complex, which causes reduction in electron density on phosphorus center. Furthermore, to confirm the binding events of PPi with **R1**complex; the FTIR spectra of pure pyrophosphate and **R1**+ PPi aggregates were recorded (Figure S28**)**. FTIR spectra of pure pyrophosphate exhibit stretching vibration frequency at 1093and 914 cm^{-1} corresponding to P=O and O-P–O bond. The FTIR spectra of aggregates exhibit vibration frequency at 3440, 1625, 1436, 1062, 880 cm^{-1}attributed to -NH, -C=N, C=C, P=O and O-P–O bonds, respectively. Thus, it is observed that on the binding of pyrophosphate to **R1** complex, the stretching vibration frequency of P=O bond and O-P–O bond shifted to lower frequency side. It is due to the P=O, and O-P–O bond binds with the zinc metal ion and cause a decrease in the strength of P=O and O-P–O bonds. The powder XRD pattern of aggregates was also recorded to check the effect of pyrophosphate binding on the crystallinity of zinc complex (Figure S29**)**. The powder XRD pattern of aggregates had shown broad peak which is due to semi-crystalline or amorphous state. These changes in the physical state indicate that the aggregation reduces the crystallinity of zinc complex.[59] Thus, based on all characterization data the possible sensing mechanism of PPi is shown in Figure S30.

Detection of Intracellular PPi and Imaging

Pyrophosphate is one of the important biological anions, as it demonstrates an intense role in many cellular processes.[60,61] Therefore, it has led to the remarkable interest of analytical chemist to synthesize such sensor which can detect PPi in the biological system. Herein, we report the intracellular detection of pyrophosphate with **R1** in HeLa cells using fluorescence microscopy. The HeLa cells were incubated with 10 μM of **R1** for 2 hours followed by three times washing with phosphate-buffered saline (PBS) and fixed with 4 % paraformaldehyde. The cover-slip was further mounted over microscopic slides, and images of the cells were recorded as shown in Figure 4 The investigations corroborate that HeLa cells shows blue emission on treatment with **R1**, which attributed to intracellular detection of pyrophosphate. Fascinatingly, as revealed in Figure 4, the nucleus of HeLa cell is deeply blue stained as compared to the cytoplasm. This means that the **R1**, complex principally stain the nucleus of HeLa cell. However, we cannot rule out the staining of cytoplasm of HeLa cell by **R1**. Thus, the cell imaging studies confirm that the complex **R1** could be used for pyrophosphate sensor in living cells. The cytotoxicity is among one of major concern which is related to developing of sensor system for biological relevance. It is well familiar that most transition metal complex based sensors have shown toxicity to cells over some interval of time. Therefore, the metal complexes used for cell tracking and cell imaging must have minimum cell toxicity. The cell viability assay for zinc complex **R1** and **R1**+ PPi were evaluated using MTT assay with HeLa and MCF-7 cell cultured in growth medium. The HeLa and MCF-7 cell were cultured in MEM media nutrient (Antimycotic) with 10 % fetal bovine serum at 37 °C for 24 hours in 5 % carbon dioxide environment. The zinc complex **R1** (10 μM) along with cell (HeLa and MCF-7 cell) incubated at 37 °C for 4 hours and observation shows 80 - 85 % cell viability. Also, to ensure the cytotoxicity of tested complexes the dose-dependent studies were carried out. The investigation affirms 75- 80 % of cells keep on viable in the concentration range of 25-80 μM as shown in Figure S31A–B.

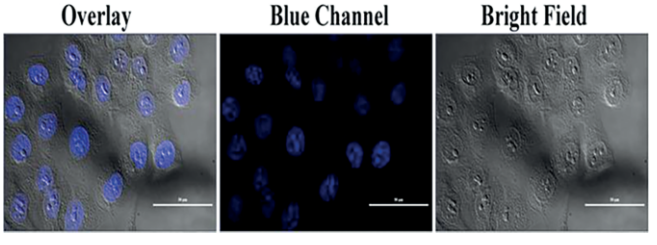

Figure 4. Fluorescence images of Hela cells showing nuclear staining (blue emission) on treatment with complex **R1**.

Alkaline Phosphatase (ALP) Activity

Phosphorylation reaction plays an essential role in many biological processes like energy transduction, gene expression, and cell signaling.[62] Most of the phosphorylation reaction are very slow and enzyme can accelerate such reaction under relevant biological condition.[63] The enzymatic reactions are proceeded

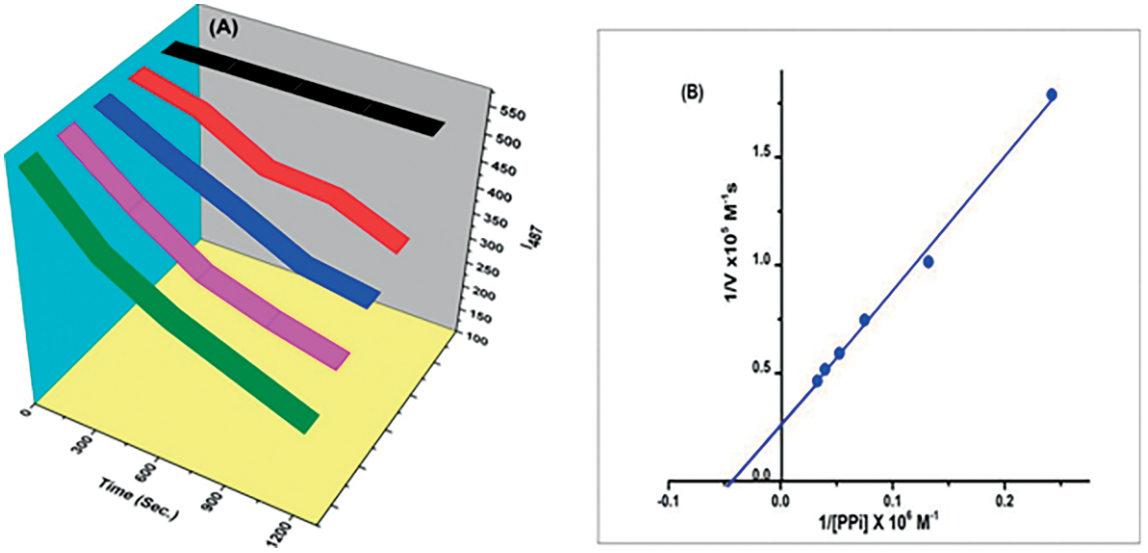

Figure 5. (A) The 3D ribbon diagram of real-time ALP activity having 10 μM of **R1**+30 μM of PPi (λ_{ext} = 310 nm, λ_{emi} = 487 nm); (B) Lineweaver–Burk plot for the hydrolysis of R1+PPi complex by ALP enzyme.

through stable transition state and thus fast. Therefore, the basic understanding of such reaction is important which are stabilized by transition state.[64] Alkaline phosphatase **(ALP)** is the enzyme that containing two zinc atom for its catalytic center and active at basic pH.[65] ALP is regularly used enzyme for diagnosis of numerous diseases especially related to liver and bone.[66] It is also employed as a biomarker for liver disease in various pathological laboratory.[67]Here, we report the PPi based zinc complex as a bio-analytical tool to construct real-time fluorescence "OFF" assay for ALP. In the control experiment, a solution of 10 μM **R1**, 30 μM of PPi and 10 μM of Tris-HCl buffer (pH = 8.3) was prepared and incubated for 30 minutes at 37 °C. The varying concentration of ALP was added to above solution, and emission response was observed at 487 nm with respect to time (0-20 minutes). It could be observed from Figure 5A that the emission intensity of **R1+ PPi** complex at 487 nm, starts decreasing with increase in the time interval. However, ALP has a very little effect on the emission intensity of the **R1** complex as in Figure S32. This examination indicates that the fluorescence intensity of **R1** decline due to consumption of pyrophosphate by ALP enzyme. More prominently, the extent of decrease in the emission intensity indicates that ALP concentration increases with an increase in the time interval. The turbidity of **R1** + PPi solution in the presence of ALP was checked with different time interval. The investigation shows that the turbid solution become transparent after 40 minute that also confirms the consumption of pyrophosphate by ALP enzyme in the solution (Figure S33). Time-dependent emission spectra was used to scrutinize the kinetics of the hydrolysis reaction under fixed ALP concentration (20 nM). The initial rate of ALP catalyzed reaction was determined from the fluorescence titration experiment. Further, a non-linear regression plot between initial rates (V_o) vs. different concentration of pyrophosphate (5 to 30 μM) was made in GraphPad Prism7 window software (Figure S34). The plot indicates that the straight line is observed at initial enzyme concentration. However, at saturated enzyme concentration the rate is diverted from the straight line. Further, initial rate law data was fitted into GraphPad Prism 7 program and Lineweaver–Burk fitting model was applied (Figure 5B). The fitting data provided the value of V_{max} = 3.696 μM min^{-1}, K_m = 17.43 × 10^{-4} M and K_{cat} = 38.4 min^{-1}, respectively. Hence, it is depicted from the Michaelis–Menten parameter that the hydrolysis reaction proceeded by the single enzyme-substrate intermediate. This has also been reported that the active unit of ALP consists of two dinuclear zinc ions and the arginine group of ALP can undergo orientation change and interact with substrate to provide serine alkoxide residue for hydrolysis of pyrophosphate through covalent enzyme-phosphate intermediate. Further, this intermediate was hydrolyzed in the second step of the reaction.[42,68] Hence, it is concluded from this studies that the R1 + PPi solution could be used for real-time fluorescence turn- OFF sensor for ALP.

Conclusions

We have synthesized and utilized two benzimidazole-based zinc complexes for sensing of pyrophosphate at physiological pH. Complex **R1** shows selective detection of pyrophosphate, which was corroborated by the emission spectrum. The emission spectra of **R1** exhibit 5.5-fold enhancement on binding with pyrophosphate, which is attributed to aggregation-induced emission. The pyrophosphate induced aggregation of complex **R1** was further investigated with microscopic studies. Facilitating sensing in the aqueous phase, complex **R1** was also utilized for PPi detection in HeLa cells imaging and cytotoxicity studies. The cell imaging experiments demonstrate that the **R1** complex senses pyrophosphate in the intracellular system. Complex **R2** shows binding with PPi and other nucleotides, which seems to be due to the chelate effect. The real sample analysis of complex **R1** was executed for the enzymatic activity of ALP. The result of ALP activity illustrates the decrease in fluo-

rescence intensity of **R1** + PPi at 487 nm related to time. It is due to the progressive consumption of PPi in the reaction mixture by ALP. Thus, complex **R1** acts as a bio-analytical tool to construct real-time fluorescence "OFF" assay for ALP.

Experimental Section

General Information: All the chemicals used for this manuscript are of analytical grade and purchased from Sigma Aldrich co., Avra, and SD Fine India. ^{1}H and ^{13}C NMR spectra were recorded on JEOL instrument operated at 400 MHz for ^{1}H NMR, 100 MHz for ^{13}C NMR and 160 MHz for ^{31}P NMR spectroscopy. FTIR spectra of a dried sample of both ligands (**L1-2**) and their zinc complexes **R1-2** were measured on a Bruker Tensor 27 spectrophotometer using a solid cell. Elemental analysis was monitored through a Fisons instrument (Model EA 1108 CHN). Powder XRD pattern was measured on a PAN analytical X'PERT PRO diffractometer using Cu-K_α radiation (λ = 0.1542 nm, 40 kV, 40 mA) and a proportional counter detector in the 2θ range of 5°–80° with a scan speed of 2°min^{-1}. TGA was performed on a Mettler Toledo thermogravimetric analyzer under a nitrogen atmosphere in the temperature range 25–700 °C (heating rate = 10 °C min^{-1}). UV/Visible absorption and Fluorescence emission spectra were recorded on a Shimadzu UV-2600 and Perkin L55 instrument, respectively. The absorption and emission spectra were measured in the fixed wavelength range of 200-700 nm at room temperature using quartz cuvette with a 1 cm path length. Dynamic Light Scattering (DLS) was used to measure the particle size of nanoaggregates with external probe feature of Metrohm Microtrac Ultra Nanotrac Particle Size Analyzer. TEM studies were performed on a Hitachi (H-7500) instrument working at 120 kV and a 400-mesh; carbon-coated copper grid was used for sample preparation. The surface morphology and size of aggregates were measured with Bruker scanning probe microscope. Fluorescence lifetimes of all complexes were recorded with Pico Quant FluoTime 300 High-Performance Fluorescence Lifetime Spectrometer using time-correlated single photon counting (TCSPC) technique. The multiexponential function was used to measure the fitted decay profile. The response function of the instrument was determined with LUDOX as an internal reference standard.

Synthesis of Ligand L1: Ligand **L1** was synthesized via condensation reaction between *o*-phenylenediamine (540 mg, 5 mmol) and 4-pyridinecarboxaldehyde (535 mg, 5 mmol) under dilute condition maintained in ethanol as solvent (30 mL). The reaction mixture was stirred for three hours at room temperature. The dark brown colored solid product was obtained after 3hrs of reaction. The brown color product was filtered and recrystallized from ethanol to afford pure product in the form of crystals. Yield 85 %, m.p. ≥ 200 °C. FTIR (cm^{-1}) ν: 3246, 1607, 1500 and 1451;^{1}H NMR; (400 MHz, [D_6]DMSO): δ = 8.66 (m, 2 H, Ar-H, and 1 H, CH = N), 7.88 (d, 2 H, Ar-H), 7.17 (d, 1 H, Ar-H), 6.97 (t, 1 H, Ar-H), 6.70 (d, 1 H, Ar-H), 6.52 (t, 1 H, Ar-H), 5.30 (br. s, 2 H, NH_2);^{13}C NMR (100 MHz, [D_6]DMSO): δ = 154.3, 150.7, 145.2, 143.8, 134.4, 129.3, 122.6, 117.6, 116.5 and 115.4;CHN analysis: Calcd for $C_{12}H_{11}N_3$: C = 73.07, H = 5.62, N = 21.30, found in (%) C = 73.09, H = 5.51, N = 21.38, ESI-MS; (*m*/*z*) = 198.04 [M + H] $^{+}$.

Synthesis of Ligand L2: Ligand **L2** was synthesized via condensation reaction between *o*-phenylenediamine (540 mg, 5 mmol) and 4-pyridinecarboxaldehyde (535 mg, 5 mmol) in methanol solvent (5 mL). The reaction mixture was stirred for 3hrs at room temperature. After 3 hrs, a dark brownish colored solid product was obtained, which was filtered and recrystallized from CH_3OH to afford pure product. Yield 90 %, m.p. ≥ 196 °C. FTIR (cm^{-1}) ν: 3084, 1608 and 1432. ^{1}H NMR; (400 MHz, [D_6]DMSO): δ = 8.71 (d, 2 H, Ar-H), 8.06 (d, 2 H, Ar-H), 7.62 (d, 2 H, Ar-H), 7.22 (d, 2H Ar-H);^{13}C NMR (100 MHz, [D_6]DMSO): δ = 151.0, 149.3, 137.7, 123.4, 120.8, 117.8 and 115.0; CHN analysis; Calcd. for $C_{12}H_9N_3$: C = 73.83, H = 4.65, N = 21.52, found in (%) C = 73.93, H = 4.63, N = 21.43, ESI-MS; (*m*/*z*) = 196.02 [M + H] $^{+}$.

Synthesis of Complex [Zn_2 (L2)$_2$ Cl_2 (DMSO)$_2$] or R1: The complex was synthesized by preparing the solutions of $ZnCl_2$ (13.6 mg, 0.1 mmol) in 1 mL of methanol and **L1**(19.7 mg, 0.1 mmol) dissolved in 1 mL of methanol/DMSO (99:1; v/v) solvent system. Both the solutions were mixed together and stirred for one hour at room temperature. The dark brown colored solution was obtained after one hour of reaction, and the reaction mixture was filtered. The filtrate was kept for slow evaporation at room temperature and after three days, the brown colored crystals were separated out. These crystals were washed with methanol and found to be suitable for X-ray crystallographic analysis. Yield: 40 %, FTIR (cm^{-1}) ν: 3406, 1618, 1548 and 1441. ^{1}H NMR: (400 MHz, [D_6]DMSO): δ = 8.71 (d, 2 H, Ar-H), 8.06 (d, 2 H, Ar-H),7.67-7.57 (m, 2 H, Ar-H), 7.23 (br., 2 H, Ar-H);^{13}C NMR (100 MHz, [D_6]DMSO): δ = 152.5, 149.5, 133.1, 128.1, 124.0, 123.9, 122.7, 121.9, 119.3 and 112.4; Anal Calcd for C_{28} H_{30} Cl_4 N_6 O_2 S_2 Zn_2: C = 43.04, H = 3.69, N = 10.25 found in (%): C = 43.34, H = 3.25, N = 10.41.

Synthesis of Complex [$Zn(L2)_2(NO_3)_2(H_2O)_2$] or R2: The complex was synthesized by mixing the solutions of $ZnNO_3{\cdot}6H_2O$ (29.7 mg, 0.01 mmol) in methanol (1 mL) and ligand **L2** (19.5 mg, 0.01 mmol) in THF (1 mL). The solution was allowed to stir for one hour at room temperature. The obtained solution was kept for slow evaporation for two days; which generated crystals suitable for X-ray studies. Yield: 35 %, FTIR (cm^{-1}) ν: 3057, 1620, 1558 and 1456. ^{1}H NMR: (400 MHz, [D_6]DMSO): δ = 8.67 (d, 2 H, Ar-H), 8.12 (d, 2 H, Ar-H), 7.67-7.56 (m, 2 H, Ar-H), 7.22 (br., 2 H, Ar-H). ^{13}C NMR (100 MHz, [D_6]DMSO): δ = 150.7, 148.8, 135.3, 123.5, 121.2, 119.0 and 116.4; Anal Calcd for $C_{24}H_{22}N_8O_8Zn$: C = 46.81, H = 3.60, N = 18.19 found: in (%) C = 46.83, H = 3.56, N = 18.23.

X-ray Structure Determination

The X-ray diffraction data for the ligand **L1** and complexes **R1-2** were collected on a Bruker X8 APEX II KAPPA CCD diffractometer at 293(2) K using graphite monochromatized Mo-K_α radiation (λ = 0.71073 Å). The crystals positioned at 50 mm from the CCD, and the diffraction spots were measured using a counting time of 15 s. Data reduction and multi scan absorption were performed using the APEX II program suite (Bruker, 2007). The structures were solved by direct methods with the SIR97 program [S1] and refined using full-matrix least-squares with SHELXL-97[S2]. Anisotropic thermal parameters were used for all non-H-atoms. The hydrogen atoms of C–H groups were with isotropic parameters equivalent to 1.2 times those of the atom to which they were attached. All other calculations were performed using the programs WinGX [S3] and PARST [S4]. The molecular diagrams of both complexes were drawn with DIAMOND [S5] software. Final R-values along with selected refinement parameters is given in Table S1.

CCDC 1408280 (for **L1**), 1578371 (for **R1**), and 1552809 (for **R2**) contain the supplementary crystallographic data for this paper. These data can be obtained free of charge from The Cambridge Crystallographic Data Centre**.**

Evaluation of the Photophysical Properties

Photophysical properties of complex **R1** and **R2** were measured through UV/Visible absorption and emission spectroscopy. Before recording the absorption and emission spectra; the standard solu-

tion of zinc complexes (10 μM, HEPES buffer, pH = 7.4) were prepared in an aqueous medium at room temperature and used for recognition studies. All the photophysical studies were recorded in the absorption and emission wavelength range of 200 -700 nm at room temperature using 1 cm quartz cuvette.

The fluorescence quantum yield of both complexes and **R1**+PPi aggregates were measured by using the relative method. The optically matching solution of standard 2-Aminopyridine in 0.1 M H_2SO_4 (excited wavelength of 300 - 340 nm) used as a reference sample for quantum yield calculation. The fluorescence quantum yield of the complex was determined using Equation (2).

$$\Phi s = \Phi rx \frac{I}{Ir}\frac{ODr}{OD}\frac{\acute{\eta}^2}{\eta r^2} \qquad (2)$$

Whereas Φs and Φr the radiative quantum yield of sample and reference and ODr, OD is the absorbance of reference and sample respectively. Ir and I are the integrated fluorescence intensity of reference and sample, and ή and ήr are the refractive index of sample and reference solution respectively.

Chemosensor Studies: The chemosensor studies of both the complexes were performed with library of anion solutions. The10 μM solutions of complexes were made in HEPES buffer, at pH = 7.4 in aqueous system at room temperature. The 10 μM solution of complex was mixed with 30 μM of analyte in 5 mL volumetric flasks. Fourteen such solutions of zinc complexes with different anions were made and used for recognition studies. Before recording the fluorescence experiment, the solution was allowed to stand for one hour to prevent any fluctuation in the emission spectrum. The fluorescence titration experiment of zinc complexes towards pyrophosphate were performed in 1 mL cuvette. The successive addition of pyrophosphate (0- 30 μM) to **R1** complex (10 μM, HEPES buffer, pH = 7.4) was carried out and emission intensity was recorded at each addition of analyte. In order to evaluate the possible interference, the interfering analyte was added to zinc complexes in the presence of PPi and emission spectra was recorded.

Cell Cultures: The HeLa and MCF-7 cells were used in the cell images and cell viability experiments. Both cell lines purchased from National Centre for Cell Sciences (NCCS), Pune, India. The cells were grown in DMEM (Gibco™) medium supplemented with 10 % bovine serum and 1 % Antibiotic-Antimycotic (Gibco™). The cells are cultured at 37 °C in 5 % CO_2 incubator for 24 hours. The 300 μL of HeLa cells suspension was seeded in 6 well plates on a sterile cover-slip and permitted to stay for 24 hrs at 37 °C. Then, the cells were treated with 10 μM solution of zinc complex **R1** and incubated for 2 hours at 37 °C. After incubation, the cells were washed three times with phosphate-buffered saline (PBS) and fixed with 4 % paraformaldehyde. The cover-slip mounted on microscopic slides, and images of the cells recorded under Axio observer 5, Carl Zeiss Fluorescence Microscope. The cytotoxicity studies were carried out using cell growth in an exponential growth phase. The cytotoxicity studies of zinc complexes (10 μM) was conceded on HeLa and MCF-7 cells cultured in a 96-well plate and incubation at 37 °C for 24 hours. After incubation times, the 10 μL solution of HeLa and MCF-7 cells were treated with zinc complex and added to each well of the 96-well culture plate for incubation to 3 hours at 37 °C. The media decanted from the wells, and 100 μL DMSO added to each well and absorbance was measured with Tecan M200 PRO Micro Plate Reader. All the experiments were performed for three times, and the relative cell viability was express in percentage relative to the control cells.

Fluorescence Assay for ALP Activity: A purified ALP from calf intestinal mucosa used for ALP activity. The enzyme was store at -20 °C before use in the experiment. The R1+ PPi complex act as a substrate, and the stock solution was stored at 4 °C. The ALP and R1+ PPi stock solution were incubated 37 °C for 30 minutes before measuring the emission experiment. The catalytical activity of ALP (5 to 20 nM) was monitored by a decrease in the emission intensity at 487 nm for 0 to 20 minutes of time interval. All the hydrolytic reaction was studied with the effect of different substrate concentration (1 μM to 30 μM) under Tries buffer (8.3 pH), by fixed ALP concentration (20 nM). The initial rate of reaction was determined from time-dependent emission spectrum data. The Kinetic data was fitted into GraphPad Prism 7 window software and Lineweaver–Burk fitting model was applied to determine the Michaelis–Menten parameter. Fitting data gives the value of (K_m), V_{max} and K_{cat}. GraphPad Prism 7 window software is freely available online (https://www.graphpad.com) program. All the kinetic experiments were repeated for three times, and the average data was used for kinetic parameter determination.

Acknowledgments

This work was supported with a research grant from SERB-DST India, Project number EMR/2014/000613. P. R. is thankful to UGC-New Delhi for a Senior Research Fellowship. Dr. Neha Garg acknowledges financial assistance from SERB, India for Ramanujan grant (SB/S2/RJN-072/2015). Ashutosh Singh is grateful to UGC for Senior Research Fellowship.

Keywords: Zinc · Fluorescence · Sensors · Intracellular detection · ALP activity · Pyrophosphate

[1] H. He, C. Li, Y. Tian, P. Wu, X. Hou, *Anal. Chem.* **2016**, *88*, 5892–5897.
[2] Y. Mikata, R. Ohnishi, R. Nishijima, H. Konno, *Inorg. Chem.* **2016**, *55*, 11440–11446.
[3] S. Katrina, A. Jolliff, J. Yoon, S. Lee, K. K. Y. Yuen, A. Jolliffe, J. Yoon, *Chem. Soc. Rev.* **2015**, *44*, 1749–1762.
[4] L. M. Mesquita, V. André, C. V. Esteves, T. Palmeira, M. N. Berberan-Santos, P. Mateus, R. Delgado, *Inorg. Chem.* **2016**, *55*, 2212–2219.
[5] P. Sokkalingam, D. S. Kim, H. Hwang, J. L. Sessler, C.-H. Lee, *Chem. Sci.* **2012**, *3*, 1819.
[6] J. H. Kang, H. J. Kim, T. H. Kwon, J. I. Hong, *J. Org. Chem.* **2014**, *79*, 6000–6005.
[7] K. Ghosh, A. R. Sarkar, A. Samadder, A. R. Khuda-Bukhsh, *Org. Lett.* **2012**, *14*, 4314–4317.
[8] H. N. Lee, K. M. K. Swamy, S. K. Kim, J. Kwon, Y. Kim, S. Kim, Y. J. Yoon, J. Yoon, *Org. Lett.* **2007**, *9*, 5–8.
[9] K. I. M. S. Kyung, L. E. E. Dong Hoon, J. I. N. Hong, J. Yoon, *Acc. Chem. Res.* **2009**, *42*, 23–31.
[10] S. Goswami, A. K. Das, B. Pakhira, S. Basu Roy, A. K. Maity, P. Saha, S. Sarkar, *Dalton Trans.* **2014**, *43*, 12689.
[11] T. Cheng, T. Wang, W. Zhu, X. Chen, Y. Yang, Y. Xu, X. Qian, *Org. Lett.* **2011**, *13*, 3656–3659.
[12] H. N. Kim, J. H. Moon, S. K. Kim, J. Y. Kwon, Y. J. Jang, J. Y. Lee, J. Yoon, *J. Org. Chem.* **2011**, *76*, 3805–3811.
[13] Y. Zhou, Z. Xu, J. Yoon, *Chem. Soc. Rev.* **2011**, *40*, 2222–2235.
[14] Z. Xu, S. K. Kim, J. Yoon, *Chem. Soc. Rev.* **2010**, *39*, 1457–1466.
[15] M. J. Kim, K. M. K. Swamy, K. M. Lee, A. R. Jagdale, Y. Kim, S.-J. Kim, K. H. Yoo, J. Yoon, *Chem. Commun.* **2009**, 7215–7217.
[16] J. Y. Jung, E. J. Jun, Y.-U. Kwon, J. Yoon, *Chem. Commun.* **2012**, *48*, 7928–7930.
[17] Z. Xu, N. R. Song, J. H. Moon, J. Y. Lee, J. Yoon, *Org. Biomol. Chem.* **2011**, *9*, 8340–8345.
[18] H. T. Ngo, X. Liu, K. A. Jolliffe, *Chem. Soc. Rev.* **2012**, *41*, 4928–4965.

[19] S. Svane, F. Kjeldsen, V. McKee, C. J. McKenzie, *Dalton Trans.* **2015**, *44*, 11877–11886.
[20] A. Gogoi, S. Mukherjee, G. Das, *RSC Adv.* **2015**, *5*, 63634–63640.
[21] C. Caltagirone, C. Bazzicalupi, F. Isaia, M. E. Light, V. Lippolis, R. Montis, S. Murgia, M. Olivari, G. Picci, *Org. Biomol. Chem.* **2013**, *11*, 2445–2451.
[22] S. Lee, K. K. Y. Yuen, K. A. Jolliffe, J. Yoon, *Chem. Soc. Rev.* **2015**, *44*, 1749–1762.
[23] W. Fang, C. Liu, F. Yu, Y. Liu, Z. Li, L. Chen, X. Bao, T. Tu, *ACS Appl. Mater. Interfaces* **2016**, *8*, 20583–20590.
[24] Y. J. Jang, E. J. Jun, Y. J. Lee, Y. S. Kim, J. S. Kim, *J. Org. Chem.* **2005**, *70*, 9603–9606.
[25] S. Anbu, S. Kamalraj, C. Jayabaskaran, P. S. Mukherjee, *Inorg. Chem.* **2013**, *52*, 8294–8296.
[26] C. Guedes, A. A. Karande, A. J. L. Pombeiro, **2014**, https://doi.org/10.1021/ic500313m.
[27] J. Mei, N. L. C. Leung, R. T. K. Kwok, J. W. Y. Lam, B. Z. Tang, *Chem. Rev.* **2015**, *115*, 11718–11940.
[28] R. Hu, N. L. C. Leung, B. Z. Tang, *Chem. Soc. Rev.* **2014**, *43*, 4494.
[29] Y. Hong, J. W. Y. Lam, B. Z. Tang, *Chem. Soc. Rev.* **2011**, *40*, 5361.
[30] R. T. K. Kwok, C. W. T. Leung, J. W. Y. Lam, B. Z. Tang, *Chem. Soc. Rev.* **2015**, *44*, 4228–4238.
[31] J. Guo, X.-L. Li, H. Nie, W. Luo, R. Hu, A. Qin, Z. Zhao, S.-J. Su, B. Z. Tang, *Chem. Mater.* **2017**, acs.chemmater.7b00450.
[32] W. Qin, Z. Yang, Y. Jiang, J. W. Y. Lam, G. Liang, H. S. Kwok, B. Z. Tang, *Chem. Mater.* **2015**, *27*, 3892–3901.
[33] L. Chen, Y. Jiang, H. Nie, R. Hu, H. S. Kwok, F. Huang, A. Qin, Z. Zhao, B. Z. Tang, *ACS Appl. Mater. Interfaces* **2014**, *6*, 17215–17225.
[34] H. Shi, R. T. Kwok, J. Liu, B. Xing, B. Z. Tang, B. Liu, *J. Am. Chem. Soc.* **2012**, *134*, 17972–17981.
[35] S. Bhowmik, B. N. Ghosh, V. Marjomäki, K. Rissanen, *J. Am. Chem. Soc.* **2014**, *136*, 5543–5546.
[36] D. Chao, S. Ni, *Sci. Rep.* **2016**, *6*, 26477.
[37] S.-Y. Jiao, K. Li, W. Zhang, Y.-H. Liu, Z. Huang, X.-Q. Yu, *Dalton Trans.* **2015**, *44*, 1358–1365.
[38] V. E. Zwicker, B. M. Long, K. a. Jolliffe, *Org. Biomol. Chem.* **2015**, *13*, 7822–7829.
[39] X. Feng, Y. An, Z. Yao, C. Li, G. Shi, *ACS Appl. Mater. Interfaces* **2012**, *4*, 614–618.
[40] A. H. Malik, S. Hussain, A. S. Tanwar, S. Layek, V. Trivedi, P. K. Iyer, *Analyst* **2015**, *140*, 4388–4392.
[41] Z. Song, R. T. K. Kwok, E. Zhao, Z. He, Y. Hong, J. W. Y. Lam, B. Liu, B. Z. Tang, **2014**, https://doi.org/10.1021/am505150d.
[42] P. Das, N. B. Chandar, S. Chourey, H. Agarwalla, B. Ganguly, A. Das, *Inorg. Chem.* **2013**, *52*, 11034–11041.
[43] P. Das, S. Bhattacharya, S. Mishra, A. Das, *Chem. Commun.* **2011**, *47*, 8118–8120.
[44] K. Wang, J.-H. Cui, S.-Y. Xing, H.-X. Dou, *Org. Biomol. Chem.* **2016**, *14*, 2684–2690.
[45] S. Li, C. Li, Y. Li, J. Fei, P. Wu, B. Yang, J. Ou-yang, S. Nie, **2017**, https://doi.org/10.1021/acs.analchem.7b01351.
[46] J. G. Zalatan, L. Catrina, R. Mitchell, P. K. Grzyska, P. J. O'Brien, D. Herschlag, A. C. Hengge, *J. Am. Chem. Soc.* **2007**, *129*, 9789–9798.
[47] E. E. Kim, H. W. Wyckoff, *J. Mol. Biol.* **1991**, *218*, 449–464.
[48] G. Li, H. Fu, X. Chen, P. Gong, G. Chen, L. Xia, H. Wang, J. You, Y. Wu, *Anal. Chem.* **2016**, *88*, 2720–2726.
[49] H. Sharma, N. Singh, D. O. Jang, *Green Chem.* **2014**, *16*, 4922–4930.
[50] H. Sharma, N. Kaur, N. Singh, D. O. Jang, *Green Chem.* **2015**, *17*, 4263–4270.
[51] Z. Zhou, W. Li, X. Hao, C. Redshaw, L. Chen, W. H. Sun, *Inorg. Chim. Acta* **2012**, *392*, 345–353.
[52] A. Singh, S. Kaur, N. Singh, N. Kaur, *Org. Biomol. Chem.* **2014**, *12*, 2302–2309.
[53] A. Singh, P. Raj, N. Singh, *ACS Appl. Mater. Interfaces* **2016**, *8*, 28641–28651.
[54] P. Raj, A. Singh, K. Kaur, T. Aree, A. Singh, N. Singh, *Inorg. Chem.* **2016**, https://doi.org/10.1021/acs.inorgchem.6b00332.
[55] H. Ju, D. J. Chang, S. Kim, H. Ryu, E. Lee, I. H. Park, J. H. Jung, M. Ikeda, Y. Habata, S. S. Lee, *Inorg. Chem.* **2016**, *55*, 7448–7456.
[56] M. Shyamal, P. Mazumdar, S. Maity, S. Samanta, G. P. Sahoo, A. Misra, *ACS Sens.* **2016**, *1*, 739–747.
[57] S. S. Mati, S. Chall, S. Konar, S. Rakshit, S. C. Bhattacharya, *Sens. Actuat. B Chem.* **2014**, *201*, 204–212.
[58] A. Gogoi, S. Mukherjee, A. Ramesh, G. Das, *Anal. Chem.* **2015**, *87*, 6974–6979.
[59] A. Wang, R. Fan, P. Wang, R. Fang, S. Hao, X. Zhou, X. Zheng, Y. Yang, *Inorg. Chem.* **2017**, *56*, 12881–12892.
[60] A. D. Cabral, B. I. Murcar-Evans, K. Toutah, M. Bancerz, D. Rosa, K. Yuen, T. B. Radu, M. Ali, A. Penkul, D. Kraskouskaya, et al., *Analyst* **2017**, https://doi.org/10.1039/C7AN00722A.
[61] B. Naskar, R. Modak, D. K. Maiti, M. G. B. Drew, A. Bauza, A. Frontera, C. Das Mukhopadhyay, S. Mishra, K. Das Saha, S. Goswami, *Dalton Trans.* **2017**, *46*, 9498–9510.
[62] H. Liu, M. Li, Y. Xia, X. Ren, *ACS Appl. Mater. Interfaces* **2016**, acsami.6b11920.
[63] C. Lad, N. H. Williams, R. Wolfenden, *Proc. Natl. Acad. Sci. USA* **2003**, *100*, 5607–5610.
[64] K. M. Holtz, B. Stec, R. Kantrowitz, E. R. Kantrowitz, *J. Biol. Chem.* **1999**, *274*, 8351–8354.
[65] S. H. Jung, K. Y. Kim, J. H. Lee, C. J. Moon, N. S. Han, S. J. Park, D. Kang, J. K. Song, S. S. Lee, M. Y. Choi, et al., *ACS Appl. Mater. Interfaces* **2017**, *9*, 722–729.
[66] D. Shi, Y. Sun, L. Lin, C. Shi, G. Wang, X. Zhang, *Analyst* **2016**, *141*, 5549–5554.
[67] K. Ooi, K. Shiraki, Y. Morishita, T. Nobori, *J. Clin. Lab. Anal.* **2007**, *21*, 133–139.
[68] M. H. Le Du, T. Stigbrand, M. J. Taussig, A. Ménez, E. A. Stura, *J. Biol. Chem.* **2001**, *276*, 9158–9165.

Received: September 24, 2018

Fluorescence Bioimaging

P. Raj, A. Singh, A. Singh, A. Singh, N. Garg, N. Kaur, N. Singh** 1–12

Pyrophosphate Prompted Aggregation-Induced Emission: Chemosensor Studies, Cell Imaging, Cytotoxicity, and Hydrolysis of the Phosphoester Bond with Alkaline Phosphatase

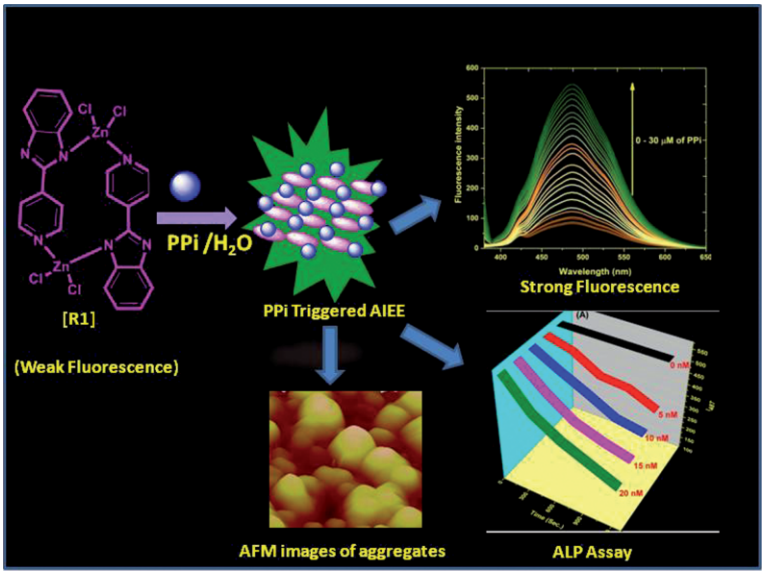

We have designed and synthesized two benzimidazole-based zinc complexes for pyrophosphate sensing in aqueous media. One of the complexes also shows pyrophosphate sensing in Hela cells. It is also used as a bioanalytical tool to construct a real-time fluorescence assay for the enzymatic activity of alkaline phosphatases (ALP).

DOI: 10.1002/ejic.201801173